

Simple 3D Pose Features Support Human and Machine Social Scene Understanding

Wenshuo Qin, Leyla Isik; Johns Hopkins University

Abstract

Humans can quickly and effortlessly extract a variety of information about others' social interactions from visual input, ranging from visuospatial cues like whether two people are facing each other to higher-level information. Yet, the computations supporting these abilities remain poorly understood, and social interaction recognition continues to challenge even the most advanced AI vision systems. Here, we hypothesized that humans rely on 3D visuospatial pose information to make social interaction judgments, which is absent in most AI vision models. To test this, we combined state-of-the-art pose and depth estimation algorithms to extract 3D joint positions of people in short video clips depicting everyday human actions and compared their ability to predict human social interaction judgments with current AI vision models. Strikingly, 3D joint positions outperformed most current AI vision models, revealing that key social information is available in explicit body position but not in the learned features of most vision models, including even the layer-wise embeddings of the pose models used to extract joint positions. To uncover the critical pose features humans use to make social judgments, we derived a compact set of 3D social pose features describing only the 3D position and direction of faces in the videos. We found that these minimal descriptors matched the predictive strength of the full set of 3D joints and significantly improved the performance of off-the-shelf AI vision models when combined with their embeddings. Moreover, the degree to which 3D social pose features were represented in each off-the-shelf AI vision model predicted the model's ability to match human social judgments. Together, our findings provide strong evidence that human social scene understanding relies on explicit representations of 3D pose and can be supported by simple, structured visuospatial primitives.

Introduction

Humans can instantly and effortlessly recognize whether two people are socially interacting. This capacity is a core human ability, and growing research in psychology and neuroscience suggests that this ability depends on extracting visuospatial cues, such as positions, orientations, and motion of bodies, which provide the building blocks for higher-level inferences about others' beliefs and goals (McMahon & Isik, 2023; Papeo, 2020; Scholl & Gao, 2013). Many of these abilities are present in infancy (Hamlin et al., 2007; Spelke, 2022; Thomas, 2024) and are also shared with nonhuman primates (Krupenye & Hare, 2018). Despite its importance, the computational processes that support social interaction perception remain unknown. Traditional studies of visual processing have largely focused on individual objects and scenes. In contrast, social understanding requires a different hierarchical structure (McMahon et al., 2023), yet precisely what spatial and dynamic features make social interactions recognizable, and how these features might be represented in computational models, remain open questions.

At the same time, modern artificial neural networks have made rapid advances in recognizing objects, scenes, and actions. Deep neural networks (DNNs) trained on large-scale image and video datasets can match or exceed human accuracy on many general vision tasks like object and categorization, segmentation, scene captioning, etc. Yet these mass trainings still do not match human social understanding (Lake et al., 2017; Netanyahu et al., 2021; Shu et al., 2021). For example, a recent study showed that while pretrained DNNs align with human judgments of physical and scene features, they diverge markedly from human judgments of social features, such as identifying whether two people are facing one another or engaged in a social interaction (Garcia et al., 2024). This suggests that the representations learned by current vision models, even in modern large-scale self-supervised models, miss key visuospatial information that humans rely on to recognize social interactions.

One possibility is that human social judgments rely on interpersonal relation information, such as the gaze patterns and physical contact between people, and that this information is largely lacking in the learned embeddings of most vision models. Recent work has shown that simpler cognitively based models, recurrent and graph neural networks that get explicit information about agents and their visuospatial relational gaze information, can rival these state-of-the-art models with a fraction of the training data and learnable parameters, highlighting the importance of visuospatial relations for human social judgments (Malik & Isik, 2023; Qin et al., 2025). However, neural network approaches in general still face critical limitations (Bowers et al., 2023; McCloskey, 1991). Artificial neural networks, even those with cognitive priors, lack interpretability, and the visuospatial cues in prior social models are not image-computable and often depend on manually annotated inputs.

In the current study, we seek to overcome these limitations by using explicit and interpretable representations that directly capture the 3D visuospatial information about people in the scene in image-computable models. We test two central hypotheses: (1) that humans rely on 3D pose

information to make social interaction judgments, and (2) that this information is missing in most modern vision DNN models. To test these hypotheses, we use a dataset of short naturalistic video clips depicting two people engaged in everyday actions, each annotated with human ratings along dimensions that span from low-level scene perception to higher-level social interaction judgments (McMahon et al., 2023). We combine state-of-the-art computer vision models to extract 3D joint and depth information from the videos and ask how well these predict human social judgments. We then ask whether the dense 3D joint information can be reduced to simple visuospatial features based on cognitive theories that capture each agent’s position and facing direction in 3D space (McMahon & Isik, 2023; Zhou et al., 2019). Finally, we evaluate how well these explicit geometric representations account for human judgments compared with the learned embeddings of diverse off-the-shelf vision DNN models, including diverse image-based and video-based architectures.

Together, this work sheds important light on the representational basis of human social vision and suggests new directions for building machine systems that reason about the social world through simple, structured geometric representations.

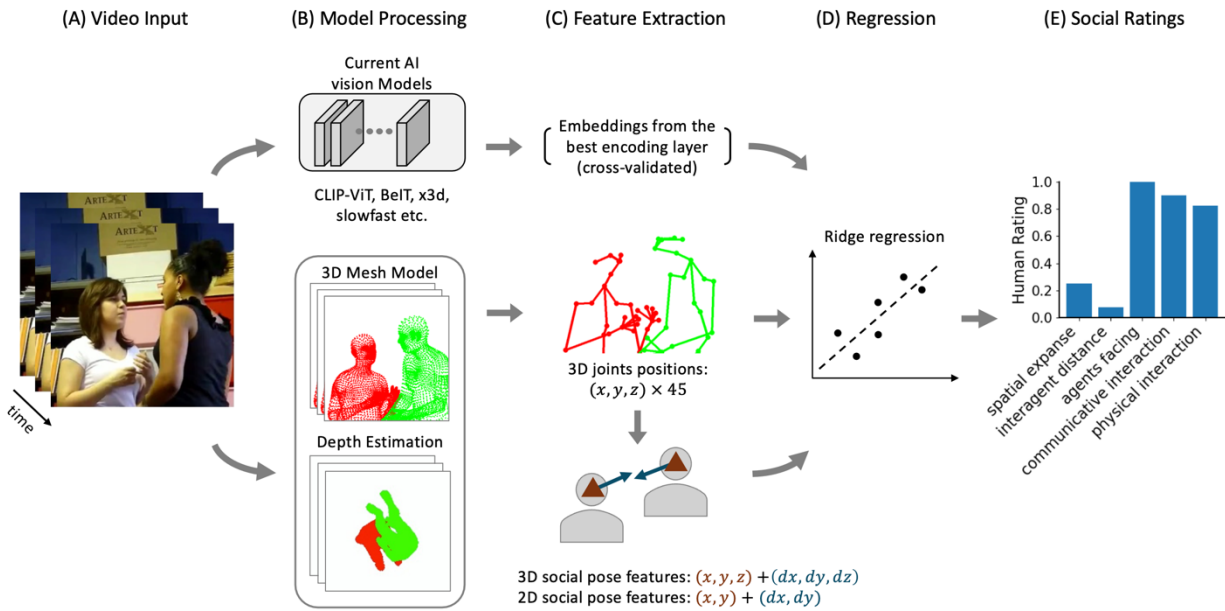


Figure 1: Overview of the video-based social rating prediction pipeline. (A) Video frames from a naturalistic dyadic interaction dataset are processed through (B) either AI vision models (e.g., CLIP-ViT, BeiT, x3d, slowfast) to extract learned visual embeddings (top), or the proposed 3D mesh modeling pipeline that combines a 3D mesh model and a pose depth estimation model for reconstructing body geometry with accurate depth estimation (bottom). (C) Feature extraction yields embeddings from the best encoding layer of each vision model (determined via cross-validation, top) or explicit 3D joint positions (x, y, z) for 45 body keypoints (middle). From these joints, we derive compact 3D social pose features capturing each agent’s head position (x, y, z)

and facing direction (dx, dy, dz) in 3D space and their 2D projections (x, y) + (dx, dy) (bottom). (D) Separate ridge regressions map each feature set to (E) five human-rated behavioral dimensions: spatial expanse (scene size), interagent distance (distance between agents), agents facing (the extent to which people are oriented towards or away from each other), communicative interaction (whether people are communicating), and physical interaction (whether people are acting together physically). Each feature set was evaluated on the Pearson correlation score between the model predicted ratings and the actual human ratings.

Results

Explicit 3D Joint Positions Exceed Most AI Vision Model Embeddings in Predicting Social Interaction Features

We compared 3D joint positions and layer-wise embeddings from different off-the-shelf vision models in their ability to predict human judgments of short video clips (Figure 1). We used a dataset of 250 three-second, silent videos depicting two people engaged in natural, everyday actions, drawn from the *Moments in Time* action recognition dataset (McMahon et al., 2023; Monfort et al., 2020), each annotated with behavioral ratings on spatial expanse (scene size), interagent distance (distance between two people), agents facing (whether or not people are facing each other), communicative interaction (whether or not people are communicating), and physical interaction (whether or not people are acting together). We first replicated prior findings that while most pretrained vision models—including static image networks (e.g., BeIT, SimCLR) (Bao et al., 2021; Chen et al., 2020), language-aligned multimodal models (e.g., CLIP-ViT) (Radford et al., 2021), and video models (e.g., X3D, TimeSformer) (Bertasius et al., 2021; Feichtenhofer, 2020) (for a full list, see Supplemental Table 1)—can match human judgments of scene features (i.e., spatial expanse), they show gaps in their ability to make human social judgments, such as interagent distance, agents facing, communicative interaction, and physical interactions.

We next asked how well the full-body 3D joint positions for the two people, averaged across frames of each video, could predict human judgments. Across all five behavioral ratings, 3D joint positions consistently outperformed the mean prediction accuracy of off-the-shelf vision models ($\Delta r = 0.0545$ for spatial expanse, 0.0526 for interagent distance, 0.2503 for agents facing, 0.0858 for communicative interaction, and 0.2640 for physical interaction; Fig. 2). This advantage was especially pronounced for agents facing where 3D joint positions significantly exceeded Vision DNN embeddings ($p = 0.0348$, two-tailed permutation test). Surprisingly, this advantage could not be seen in the internal representations of the pose model used to generate 3D joint positions, as the best layer from the 3D joint pose model, 4D Humans (Goel et al., 2023), performed worse than the mean of standard vision DNNs and the explicit 3D joint positions across all behavioral dimensions.

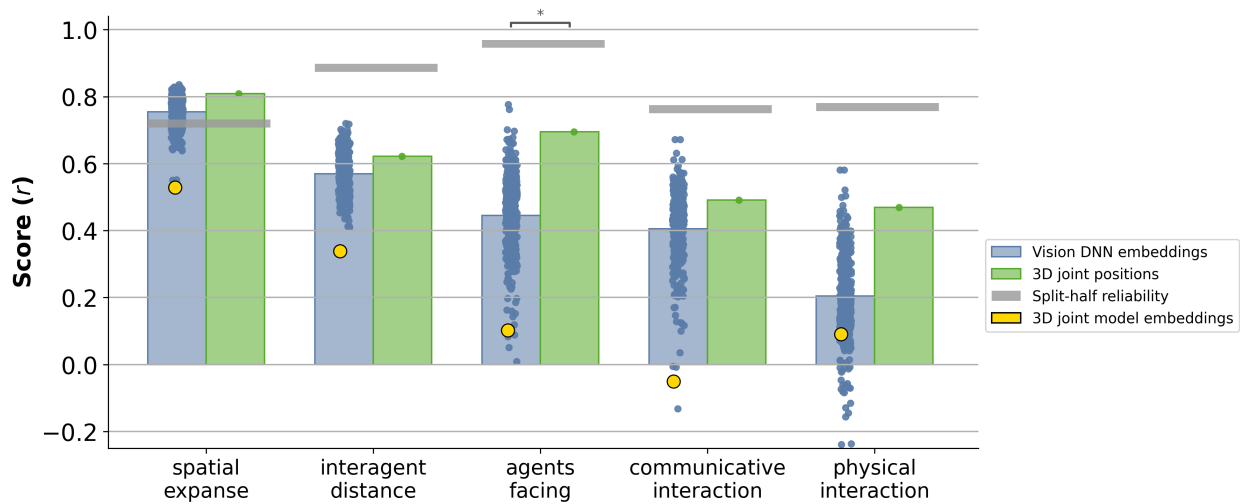


Figure 2: Vision DNNs and 3D Joint Position Prediction of Human Social Ratings.

Comparison of Vision DNNs (blue), 3D joint positions (green), and the 3D joint model embeddings (yellow) performance in predicting different human social scene ratings. Score is measured as the Pearson correlation (r) between the predicted and the true human ratings across five dimensions: spatial expanse, interagent distance, agents facing, communicative interaction, and physical interaction. The average performance was shown in bars. Each dot in the vision DNN embeddings shows the performance of the model's best layer (cross-validated) for each judgement. Similarly, the yellow star represents the best layer performance of the 3D joint model. Gray horizontal bars indicate the split-half reliability of human ratings. Asterisks mark significance levels from two-tailed non-paired permutation tests ($*p < 0.05$).

Simple 3D Social Pose Features Match Dense 3D Joint Positions in Predicting Social Ratings

To determine whether the predictive power of 3D joint positions could be captured by a simpler and more interpretable representation, we generated a compact set of 2D and 3D social pose features that encode only each agent's position and facing direction. Across all five behavioral dimensions, the compact 3D social pose features performed nearly identically to the full set of 3D joints ($\Delta r = 3D \text{ joints} - 3D \text{ social pose features} = +0.0122$ for spatial expanse, $+0.0290$ for interagent distance, -0.0214 for agents facing, $+0.0301$ for communicative interaction, and -0.0880 for physical interaction; Fig. 3).

In contrast, 2D social pose features, which lack depth information, showed a consistent reduction in performance relative to the full 3D joints ($\Delta r = 3D \text{ social pose features} - 2D \text{ social pose features} = +0.5459$ for spatial expanse, $+0.3218$ for interagent distance, $+0.0629$ for agents facing, and $+0.2493$ for communicative interaction), highlighting the importance of 3D visuospatial information.

Consistent with these results, semi-partial correlation analyses (Supplementary Fig. S1) confirmed that if 3D social poses are controlled for, the full 3D joint positions contribute little additional prediction to human social features.

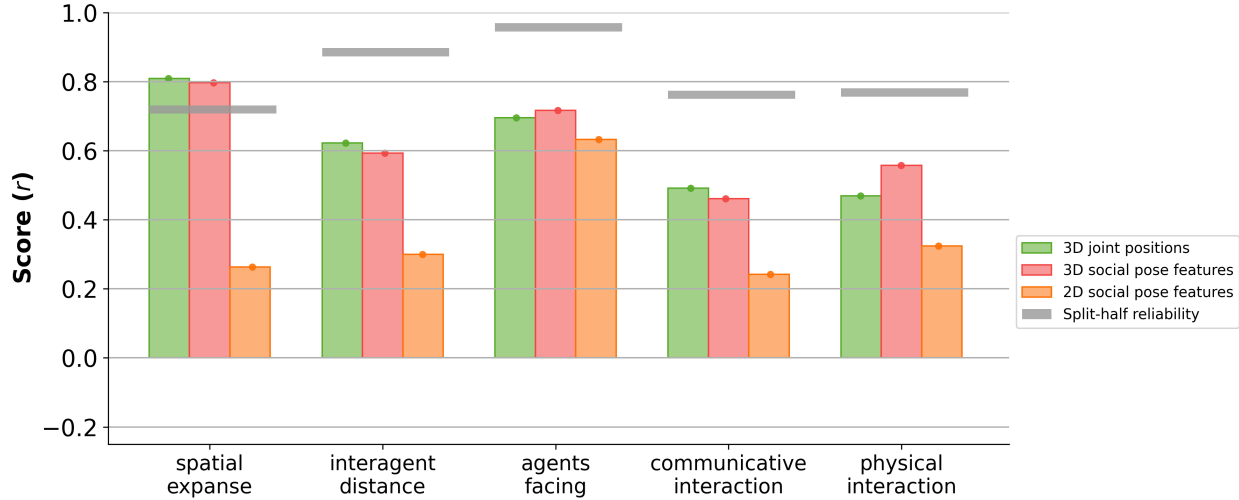


Figure 3: Compact 3D Social Pose Features Match Full 3D Joint Positions and Rival Vision DNNs. Comparison of 3D joint positions (green), 3D social pose features (red), and 2D social pose features (orange). Score is measured as the Pearson correlation (r) between the predicted and the true human ratings across five dimensions: spatial expanse, interagent distance, agents facing, communicative interaction, and physical interaction. Gray horizontal bars indicate the split-half reliability of human ratings.

3D Social Pose Features Augment Modern Vision DNNs' predictions of Human Judgments

To test whether 3D social pose information provides complementary information to modern vision models, we combined the 3D social pose features with the embeddings from a large set of vision DNNs using grouped ridge regression and evaluated their joint predictive power for human social judgments. Across all five behavioral ratings, adding 3D social pose features to vision DNN embeddings significantly improved prediction performance (Fig. 4; $p < 0.001$ for all ratings, paired one-tailed permutation test). A substantial proportion of models shows improvement for each rating: spatial expanse, 324 of 351 models ($\Delta r = 0.0621$); interagent distance, 304 of 351 ($\Delta r = 0.0835$); agents facing, 349 of 351 ($\Delta r = 0.2906$); communicative interaction, 322 of 351 ($\Delta r = 0.1501$); and physical interaction, 232 of 351 ($\Delta r = 0.0832$). These results show that not only can simple 3D pose features match the performance of current vision DNNs, but they also provide information that is not captured in the learned embeddings of most modern models.

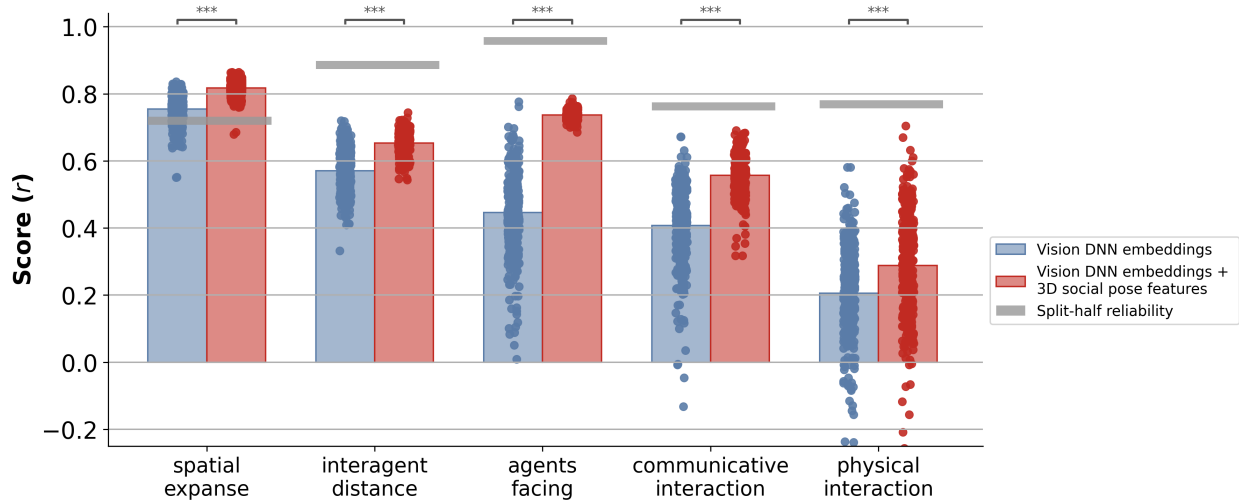


Figure 4: 3D Social Pose Features Enhance Vision DNN Predictions of Human Social Judgments. Comparison of Pearson correlations (r) between (1) Vision DNN embeddings alone and (2) Vision DNN embeddings combined with 3D social pose features. Each dot represents one model's best layer's prediction. Bars indicate group means. Gray horizontal bars indicate the split-half reliability of human ratings. Asterisks denote significance levels from one-tailed paired permutation tests ($***p < 0.001$).

Off-the-shelf Vision DNNs that Encode 3D Social Pose Features Better Predict Human Social Judgments

Finally, we examined whether the degree to which off-the-shelf vision DNNs represent 3D social pose information relates to their ability to predict human judgments of social interactions. For each model, we selected the layer that best predicted each human social behavioral rating and evaluated how well that layer's embeddings predicted the 3D social pose features. Across all social ratings, models that more strongly encoded 3D social pose features tended to achieve higher alignment with human judgments, particularly for interagent distance, agents facing, communicative interaction, and physical interaction. These dimensions showed positive relationships ($r = 0.39, 0.66, 0.52, 0.32$), whereas spatial expanse, a more scene-centric rating, showed no clear trend ($r = 0.01$). In contrast, when the same analysis was performed using 2D social pose features, the relationships were overall weaker across all ratings. The correlation with spatial expanse was negative ($r = -0.12$), and the associations for interagent distance, agents facing, communicative interaction, and physical interaction all decreased ($r = 0.22, 0.45, 0.36, 0.20$).

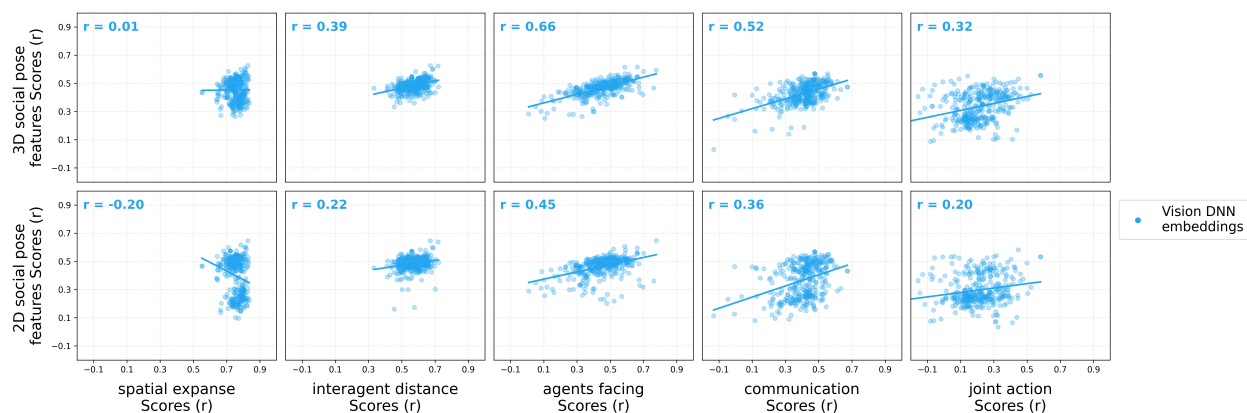


Figure 5: Vision DNNs that Better Encode 3D Social Pose Features Better Predict Human Social Judgments. Each scatterplot shows, for every Vision DNN model, the performance of its best layer in predicting human social feature ratings (x-axis) versus its ability to predict 3D or 2D social pose features (y-axis). Each dot represents one model’s best layer, which is determined through cross-validation based on its prediction of human ratings, and that same layer is then evaluated on social pose features. The regression line indicates the overall trend, and the top left correlation coefficient (r) indicates the strength of the relationship between the two prediction accuracies.

Discussion

In this study, we tested whether explicit 3D body geometry can account for human social judgments and complement the representations learned in modern DNNs. Across multiple human social scene judgements, we found that simple 3D pose-based representations, both the full body 3D joint positions and a compact set of 3D social pose features, rival or surpass the performance of modern AI vision models. These findings suggest that much of human social scene understanding can be supported by explicit, low-dimensional geometric primitives, and that this information is lacking in most modern vision DNNs.

3D Joint Positions Match Top Vision Models in Social Interaction Prediction

Explicit 3D joint positions consistently outperformed the average of off-the-shelf vision models across all behavioral dimensions, with advantages for socially relevant features like agents facing and physical interaction. This reveals that critical social information is available in explicit body geometry but not adequately captured in the learned representations of most vision models, even those trained on massive datasets with sophisticated objectives, highlighting a fundamental gap in how current architectures represent visual social scenes.

Importantly, this advantage requires explicit information about 3D pose and cannot be attributed to the internal representations of the pose estimation algorithm itself. The best-performing layer

from 4D Humans, the state-of-the-art pose model used, performed worse than both the explicit 3D joints and standard vision models. This discrepancy likely arises because the internal modules of 4D Humans reconstruct full 3D body meshes by predicting parametric human body representations of both body shape and joint articulations (Goel et al., 2023). As a result, their internal embeddings are optimized for predicting mesh parameters rather than representing explicit 3D joint positions in a form suitable for linear decoding. Thus, accurate pose reconstruction does not necessarily entail interpretable geometric representations usable for social inference.

Simple Social Pose Features Capture the Predictive Power of Dense Joint Representations

The predictive power of the full 3D joint positions can be captured by a remarkably compact set of features: just the 3D position and facing direction of each agent's head. These minimal 12-dimensional descriptors ($6 \text{ dimensions} \times 2 \text{ agents}$) matched the performance of the full 270-dimensional joint representation ($45 \text{ joints} \times 3 \text{ coordinates} \times 2 \text{ agents}$). Moreover, semi-partial correlation analysis revealed that once the variance explained by these social pose features was removed, full joint positions contributed little additional predictive power.

This result aligns with cognitive theories suggesting that simple visuospatial cues like distances and orientations serve as foundational building blocks for social interaction perception (Hafri et al., 2013; Hafri & Firestone, 2021; McMahon & Isik, 2023; Papeo, 2020; Zhou et al., 2019). Even within rich, high-dimensional body configurations, social information appears to reside primarily in structured geometric primitives. In contrast, 2D pose features lacking depth information consistently underperformed, emphasizing that humans rely on explicit 3D scene geometry when recognizing social scenes. This aligns with prior work showing that the extrastriate body area (EBA), a region of human visual cortex specialized for representing bodies and their visuospatial cues (Abassi & Papeo, 2020; Downing et al., 2001; Gandolfo et al., 2024), represents information about the 3D position of bodies (Zhu et al., PNAS). This work provides some of the first empirical evidence that this 3D information is critical to downstream social tasks.

3D Social Pose Information Complements and Explains Modern Vision Model Performance

Adding 3D social pose features to vision model embeddings significantly improved prediction performance across all behavioral dimensions. The consistency of improvements across diverse architectures, convolutional neural networks (CNNs) and vision transformers (ViTs), input modalities (image and video models), and training tasks (categorization, self-supervision), suggests that the lack of explicit 3D pose information is a widespread limitation in learned embeddings of modern AI vision models.

Moreover, we found that models whose embeddings more strongly encoded 3D social pose features achieved higher alignment with human ratings, particularly for socially relevant dimensions ($r = 0.39$ for interagent distance, 0.66 for agents facing, 0.52 for communicative interaction, and 0.32 for physical interaction). However, even the best-performing models achieved correlations of only around 0.5 when predicting the 3D social pose features themselves, indicating these geometric relationships are not well represented in even the best models, and highlighting a key area for future model improvement.

These findings suggest that more human-like machine social understanding may require not only in simply scaling up current architectures, but also incorporating explicit geometric representations, which may enable more sample-efficient learning and more interpretable reasoning about spatial relationships between agents.

Limitations and Future Directions

While this study highlights key aspects of human visuospatial reasoning and limitations of modern AI, there are many outstanding future directions. First, our dataset was relatively small. Future work should incorporate longer, more diverse videos with wider distributions of spatial layouts and edge cases where geometric cues may be more ambiguous or vary in their correlations with higher-level judgements. Second, we averaged across frames in our joint position models, likely discarding rich dynamics captured in joint position, like motion synchrony and communicative exchanges. More sophisticated temporal modeling would be needed for longer videos and interactions distinguished by temporal dynamics. Third, while position and facing direction explain most linear variance in pose-based judgments, higher-level social reasoning like motivations and intentions likely require processing beyond these shallow primitives. This study also raises important questions about how the human brain represents these 3D geometric features during social perception. Recent neuroimaging suggests regions of the extrastriate body area may compute spatial relationships between agents, and encode view-invariant, three-dimensional configurations of bodies (Abassi & Papeo, 2020; Zhu et al., 2024), and transform these into higher-level judgements in the superior temporal sulcus (McMahon et al., 2023). The modeling pipeline here offers a scalable, image-computable way to systematically investigate the role of 3D visuospatial features in social brain representations.

Conclusion

Together, our findings reveal that human social scene understanding relies on explicit representations of 3D visuospatial pose information and can be supported by remarkably simple geometric primitives. These representations are largely absent from current AI vision models, explaining their continued struggles with social recognition despite impressive performance on other visual tasks. Explicitly representing spatial relationships between people may be critical for more efficient, interpretable, and human-aligned AI social reasoning. These results point toward

new architectures that combine the flexibility of deep learning with the structured efficiency of geometric reasoning, offering a path toward vision systems that see the social world more like humans do.

Methods

Behavior ratings and video dataset

We used a publicly available dataset of 250 three-second, silent videos depicting two people engaged in natural, everyday actions, drawn from the *Moments in Time* action recognition dataset (McMahon et al., 2023; Monfort et al., 2020). Each video was annotated with a comprehensive set of human behavioral ratings collected through large-scale online experiments. Participants rated each feature on a scale of 1-5, and ratings were collected and averaged for at least 10 participants.

For the present study, we focused on five rating dimensions that span a spectrum from low-level scene properties to high-level social understanding based on their importance in behavior and brain responses (McMahon et al., 2023). The first feature, spatial expanse, is a scene feature that captures the perceived size or openness of the environment. The next two features are “social primitives”, visuospatial cues that are often indicative of social interaction (McMahon & Isik, 2023): interagent distance reflects how physically close or far apart people appear within the scene, and agents facing measures the extent to which individuals are oriented toward each other. Communicative interaction captures whether agents seem to be engaged in an exchange of information or attention, such as talking, gesturing, or making eye contact, whereas physical interaction reflects whether they are engaged in direct bodily contact or coordinated joint actions, such as dancing or fighting. These dimensions provide a graded behavioral framework for evaluating how well computational models capture the visuospatial and social information humans extract from dynamic natural scenes.

The dataset was originally divided into 200 training videos and 50 test videos to facilitate cross-validated model prediction, and we maintained that pre-determined split for model evaluation. Due to occasional pose estimation failures, for instance, when one or both agents were heavily occluded, partially outside the frame, or captured in unusual body configurations, the pose model was unable to reliably extract two-person skeletons across all 90 frames for a subset of clips. To ensure high-quality and complete 3D pose data, we excluded these problematic clips, resulting in a final set of 177 training videos and 47 test videos. To maintain consistency across all analyses, this same reduced set of videos was used throughout every stage of the study.

Off-the-shelf Vision Models

We adopted the same set of vision models following the recent NeuroAI benchmarking work (Conwell et al., 2024; Garcia et al., 2024), evaluating how diverse modern vision models capture

social and spatial information from naturalistic videos. This model set included both image-based and video-based architectures spanning a range of training datasets and tasks, and architectural designs.

The image models encompassed convolutional and transformer-based architectures, such as ResNets, EfficientNets, Swin Transformers, Vision Transformers (ViTs), and CLIP variants, sourced from open repositories including Torchvision (TorchVISION maintainers and contributors, 2016), PyTorch Image Models (Timm) (Wightman, 2019), VISSL (Goyal et al., 2021), and OpenAI CLIP (Radford et al., 2021). These models were trained under a variety of objectives, including supervised classification, self-supervised contrastive learning, and multimodal vision–language alignment. In addition, we incorporated video models such as SlowFast (Feichtenhofer et al., 2019) and TimeSformer (Bertasius et al., 2021), which are specifically designed to capture temporal dynamics from short video sequences. See Supplemental Table 1 for a full list of models included.

Feature representations were extracted following the same procedures (Garcia et al., 2024) using DeepJuice (Conwell et al., 2024), a memory-efficient Python toolkit for large-scale model benchmarking. For image models, we sampled seven evenly spaced frames from each 3-second clip, processed each frame independently, and averaged their activations to obtain one embedding per video. Video models processed the full temporal sequence directly (downsampling frames based on each model’s preprocessing pipeline) to yield a single video-level representation. To enable direct comparison across models with varying dimensionalities, all extracted features were reduced to a 4,732-dimensional space via GPU-optimized sparse random projection (SRP) ($\epsilon = 0.1$), following the Johnson–Lindenstrauss lemma (Larsen & Nelson, 2014).

Depth-Aware 3D Pose and Social Feature Extraction

3D Joint Positions

We combined two state-of-the-art pose estimation algorithms to extract a set of full-body 3D joint positions. We first used the 4D Humans model, a vision transformer-based HMR 2.0 (Human Mesh Recovery v2) model that regresses human-body parameters from frames and aggregates over time for stable, consistent estimations in videos (Goel et al., 2023). The output is the parameterization of SMPL-X (Skinned Multi-Person Linear eXpressive), a detailed parametric model that represents 3D body shape and articulated pose with expressive hands and faces (Pavlakos et al., 2019).

Several videos in our dataset contain babies and children. Because of the adult-biased shape prior and training data, 4D Humans systematically pushes child-sized bodies deeper into the scene; we correct only the global translation with the BEV (“Bird’s-Eye View”) model (Sun et al., 2022). BEV estimates depth in true 3D voxels and incorporates an age-aware SMPL+A prior, making it markedly better at recovering children’s front-back position while staying robust to inter-person

occlusion (Sun et al., 2022). Accordingly, for every detection, we replace the depth component of the 4D Humans camera translation with BEV’s metric depth. This fusion keeps HMR 2.0’s high-fidelity pose/shape while inheriting BEV’s accurate, infant-aware depth ordering.

For every 90-frame clip, we used the depth-corrected SMPL-regressed 3D body joint coordinates, which output a 45-joint set including the canonical 24 SMPL body joints and 21 additional face, hand, and foot landmarks. We used the averaged 3D joint coordinates across 90 frames to predict human social ratings, allowing us to know if body pose information could explain human social judgments.

3D Social Pose Features

To identify which components of full-body joint positions drive predictions of social judgments, we designed a smaller, more interpretable set of 3D social pose features explicitly aimed at capturing the social information present in full joints. Inspired by McMahan and Isik (2023), which emphasizes distance and facing direction as foundations for social interaction recognition, we extract face position and direction for each person from full joint positions using simple, linear operations (Fig. 1C).

To construct the representation, we defined the head center as the midpoint between the two eye joints and computed a unit head-direction vector by averaging the head-center-to-nose and neck-to-nose vectors, providing both an origin on the head and an orientation consistent with the face plane and head-torso hinge. We computed both 2D and 3D versions of these features, where each 3D feature comprised (x, y, z, dx, dy, dz) and each 2D feature (x, y, dx, dy) by removing the z-dimension, capturing position and direction in their respective coordinate spaces. As with the full body joint positions, for each 90-frame clip, these features were averaged across time for each of the two people. We then used these features to assess how much of the social information in the 3D geometric pose could be captured by this compact representation and compared their predictive performance with embeddings derived from vision DNNs.

Pose Model Embeddings

To examine how the 4D Humans model represents information relevant to social interaction understanding, we also analyzed its internal latent representations. Because 4D Humans is not natively supported by the DeepJuice feature extraction framework we used for other Vision DNNs, we implemented a custom procedure to manually extract intermediate activations from the model. Specifically, we targeted two key components: the HMR2 module, responsible for estimating 3D body geometry and camera parameters from individual frames, and the PoseTransformer module, which integrates temporal information across frames to produce smooth and consistent pose trajectories. For each video, we recorded the output of every sublayer. To make these activations comparable across layers and consistent with the Vision DNNs, we applied the same SRP dimensionality reduction (4732 dimensions) implemented with the DeepJuice framework.

Encoding Framework

Ridge Encoding Model

To evaluate how well each model/feature set predicts human social judgments, we implemented a ridge regression–based encoding framework with leak-free normalization and cross-validation. We first select the best-performing layer as a representative for this model through a five-fold cross-validation repeated twice on the training set. Within each fold, both model features and behavioral ratings were z-score normalized using statistics computed from the training split and applied to both training and validation data. The regularization strength (α) was selected from a logarithmically spaced grid ranging from 10^{-10} to 10^{10} . After identifying the best-performing layer for each model, we recomputed normalization parameters on the full training data and evaluated the model on the held-out test set. Model performance was quantified as the Pearson correlation (r) between predicted and actual behavioral ratings on the test set.

For the 3D social pose features, we fit the ridge regression directly on the full training and test splits (there is no layer selection involved in the 3D features), applying the same normalization and α -selection process.

Grouped Ridge

To jointly model the contributions of vision model embeddings and 3D social pose features, we used the GroupRidgeCV implementation from the Himalaya package (Dupré la Tour et al., 2022). This method extends standard ridge regression by applying separate L2 regularization penalties to predefined feature groups, allowing the model to learn optimal weighting for the two input spaces (the vision model embeddings and the 3D social pose features), and helps account for the differences in feature set dimensionality. The optimization was performed using a random-search solver, which sampled 200 candidate group-weight configurations (γ) from a Dirichlet distribution defined on the simplex (with concentration parameters of 0.1 and 1.0) and, for each configuration, evaluated a shared set of logarithmically spaced regularization strengths from 10^{-10} to 10^{10} . All features and targets were z-score normalized before fitting. The grouped model was then trained on the full training set, and its predictive performance was evaluated as the Pearson correlation (r) between predicted and observed behavioral ratings on the held-out test set.

Semi-partial Correlation

To determine whether the concise and interpretable 3D social pose features captured all social information as the full 3D joint positions, and whether each component of 3D social pose features, which are 3D head positions and 3D orientations, was necessary, we performed a semi-partial correlation analysis. This analysis tested whether each feature set (3D head positions, 3D orientations, and their combination as 3D social pose features) explained all the variance in

behavioral ratings that was predicted by the 3D joints, or whether the full joints contained additional unique information.

We first residualized the 3D joint positions with respect to each feature set using a ridge model fit on the training data. This step removed any shared variance between the two sets of predictors, producing a residualized joint representation that contained only information not linearly predictable by the feature set. The same regression model was then applied to the test data to generate residualized test features. Then, we used ridge regression to predict the behavioral ratings from the residualized joint features. The ridge penalty parameter was selected from a logarithmic grid ranging from 10^{-10} to 10^{10} using cross-validation within the training set. Performance was evaluated on the held-out test data by computing the semi-partial correlation (r) between the predictions and the true behavioral ratings. This correlation reflects the unique contribution of the 3D joint positions beyond what was already captured by each of the feature sets.

Correlation Between Model Encodings of 3D Pose and Human Judgments

To study whether models that better encode 3D social pose information also better capture human social judgments, we correlated each model’s encoding performance across the two types of predictions. We used the same DNN encoding scores on human social judgments described above. We then measured how well the best-encoding layer selected for each human social judgment could predict the 3D social pose features using the same encoding pipelines. Therefore, for each best-performing layer, we obtained a pair of encoding scores, one for predicting human behavioral ratings and one for predicting the 3D social pose feature. We computed the correlations across all the models. The resulting relationship quantifies whether models’ ability to represent 3D social pose features is related to their success in matching human judgments.

Statistical Analyses

We performed two-tailed, non-paired permutation tests to test whether vision DNN embeddings and 3D social pose features predicted human ratings significantly differently from each other. We used the difference in the means of Pearson correlation between these two groups as the test statistic. Under the null hypothesis that both embedding groups were equally predictive, the target assignments were randomly permuted 5,000 times to generate a null distribution of mean differences expected by chance. The two-tailed p -value was then calculated as the proportion of permuted differences whose absolute value exceeded that of the observed difference.

We used a one-tailed paired permutation test in the grouped ridge analysis to evaluate whether 3D pose features could augment the encoding scores of each DNN embedding. The observed statistic was the mean paired difference in correlation scores (DNN alone minus DNN + 3D pose), with negative values indicating improved performance of the expanded models. Under the null hypothesis of no improvement, we randomly swapped 5,000 times the paired correlation

scores between the two model versions and recomputed the mean difference. Then we calculated the p -value as the proportion of permuted differences less than or equal to the observed one.

Supplemental Materials

3D Social Pose Features Capture Most Social Information from Full 3D Joint Positions

To determine whether our concise 3D social pose features (the combination of 3D head positions and 3D orientations) captured all the socially relevant information contained within the full body 3D joint positions, we performed a semi-partial correlation analysis (see Methods). This analysis tested whether the full 3D joints contained any unique predictive information beyond what was already captured by our feature sets.

We first considered the two components of our social pose features, 3D head positions and orientations, separately. When partialling out only the 3D head positions (Figure S1), the semi-partial correlations for spatial expanse ($r = 0.094$) and interagent distance ($r = 0.202$) show a clear decrease, but the correlation for agents facing ($r = 0.745$), communicative interaction ($r = 0.284$), and physical interaction ($r = 0.317$) are only minimally impacted. When partialling out only the 3D orientations (Figure S1), the semi-partial correlation did not change across all dimensions ($r = 0.798$ for spatial expanse, $r = 0.634$ for interagent distance, $r = 0.682$ for agents facing, $r = 0.437$ for communicative interaction, and $r = 0.458$ for physical interaction). The remaining predictive power in both residualized conditions demonstrated that neither 3D head positions nor 3D orientations alone was sufficient to capture all socially relevant information from the joints.

However, when the complete 3D social pose features (combining both 3D head positions and 3D orientations) were partialled out from the 3D joint positions, the unique predictive power of the remaining joint information showed dramatic drops across all five social ratings ($r = 0.070$ for spatial expanse, $r = 0.241$ for interagent distance, $r = 0.081$ for agents facing, $r = 0.035$ for communicative interaction, and $r = 0.051$ for physical interaction).

This result demonstrates that our concise 3D social pose features are both necessary (as individual components were insufficient) and largely sufficient (as the combined features left little remaining variance to be explained). The full, high-dimensional 3D joint data contains minimal unique, linearly decodable information relevant to these social ratings beyond what is already captured by our combined 3D head positions and 3D orientations.

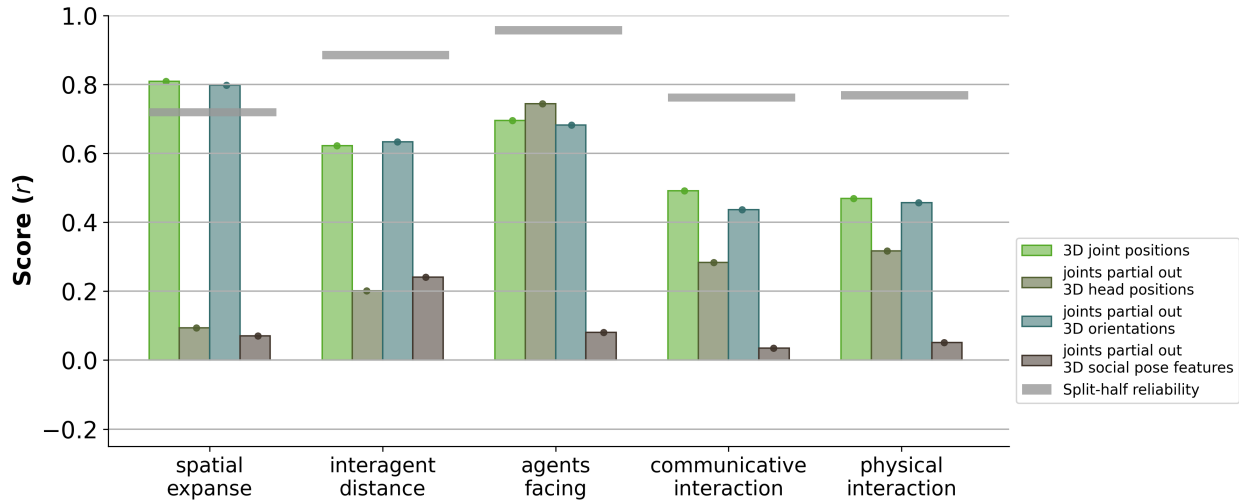


Figure S1. 3D Social Pose Features Capture Most Social Information from 3D Joint Positions. The bar chart displays the predictive performance (Pearson's r) for the full 3D joint positions (light green) and the semi-partial correlation for residualized joint features, partialling out head positions (olive), 3D orientations (teal), and the combination (dark brown). The dramatic drop in performance when the combination of position and orientation is partialled out indicates that the full body 3D joint positions contain little additional unique social information beyond the compact combination of 3D social pose features. Grey horizontal bars indicate the split-half reliability.

List of Vision DNNs Tested

model name	model type	spatial expanse	interagent distance	agents facing	communicative interaction	physical interaction
clip_vitl14	image	0.8089	0.7176	0.7763	0.6314	0.3346
clip_rn50x4	image	0.8278	0.6717	0.6973	0.53	0.5216
clip_vitb32	image	0.7556	0.6878	0.7621	0.5419	0.4581
clip_rn101	image	0.7848	0.6831	0.5918	0.5188	0.447
timm_convnext_large_in22ft1k	image	0.7506	0.6505	0.6609	0.6724	0.2791
timm_convnext_large	image	0.7506	0.6505	0.6609	0.6724	0.2791
timm_deit3_base_patch16_384_in21ft1k	image	0.8289	0.6075	0.6056	0.576	0.3739
timm_beitv2_base_patch16_224	image	0.7861	0.6293	0.701	0.4882	0.3759
timm_convnext_small	image	0.6986	0.5897	0.5889	0.5519	0.4594
timm_deit3_base_patch16_224_in21ft1k	image	0.8299	0.6927	0.6113	0.4775	0.2741
timm_deit_small_distilled_patch16_224	image	0.7813	0.7205	0.5627	0.41	0.4066
timm_deit3_large_patch16_384_in21ft1k	image	0.7746	0.6521	0.6135	0.5325	0.3066
torchvision_resnet50_imagenet1k_v2	image	0.7135	0.6175	0.6445	0.5489	0.3533
timm_convnext_large_in22k	image	0.7501	0.6328	0.6644	0.6114	0.2165
timm_gernet_m	image	0.7645	0.5981	0.6111	0.5571	0.3378
timm_beit_large_patch16_384	image	0.8143	0.7021	0.6121	0.3498	0.3796
timm_deit3_huge_patch14_224_in21ft1k	image	0.7827	0.6467	0.5848	0.5473	0.2952
timm_convnext_base_in22ft1k	image	0.8104	0.6588	0.3108	0.4839	0.5809
timm_convnext_base	image	0.8104	0.6588	0.3108	0.4839	0.5809
clip_vitb16	image	0.7587	0.6338	0.6726	0.4076	0.3687
timm_deit3_small_patch16_224_in21ft1k	image	0.7277	0.6177	0.6197	0.4813	0.3928
timm_lambda_resnet26t	image	0.7114	0.683	0.5983	0.4834	0.3542
torchvision_regnet_x_1_6gf_imagenet1k_v1	image	0.7869	0.566	0.5204	0.4735	0.4755
timm_dm_nfnet_fl	image	0.7363	0.6204	0.5701	0.574	0.2659

timm edgenext x small	image	0.7984	0.6312	0.5029	0.4619	0.3692
torchvision mnasnet1_0 imagenet1k v1	image	0.7934	0.6026	0.5335	0.5162	0.3025
torchvision regnet x 800mf imagenet1k v1	image	0.7896	0.55	0.5769	0.5841	0.244
timm deit3 small_patch16_384_in21ft1k	image	0.7346	0.6012	0.5988	0.4192	0.3879
timm convnext_base_384_in22ft1k	image	0.7988	0.66	0.5962	0.2993	0.3829
timm convnext_base_in22k	image	0.7566	0.5999	0.5026	0.4441	0.4168
timm beit_base_patch16_224	image	0.8288	0.6409	0.6313	0.4762	0.1413
timm deit3_large_patch16_384	image	0.7725	0.6467	0.5097	0.3796	0.4029
timm_legacy_seresnet50	image	0.8022	0.6505	0.5472	0.429	0.2741
slip_vit_b_yfcc15m	image	0.7981	0.6605	0.4841	0.4626	0.2939
x3d_xs	video	0.7218	0.7015	0.5197	0.3259	0.4216
timm_deit3_large_patch16_224	image	0.7904	0.5462	0.5178	0.5053	0.3288
timm_cait_xxs36_224	image	0.8049	0.6501	0.4652	0.3268	0.4379
timm_mixer_b16_224_miil	image	0.7836	0.5438	0.6205	0.4051	0.328
vicreg_resnet50_alpha0p75	image	0.7549	0.6162	0.3211	0.4895	0.499
timm_edgenext_base	image	0.7866	0.5993	0.5952	0.421	0.2736
timm_legacy_seresnext50_32x4d	image	0.7743	0.6547	0.4625	0.4463	0.3369
timm_gluon_resnet101_v1c	image	0.7346	0.6114	0.4201	0.5712	0.3359
timm_convnext_tiny	image	0.7955	0.6456	0.5452	0.4651	0.2208
timm_cait_s24_224	image	0.8094	0.6792	0.4569	0.4174	0.308
timm_convnext_pico	image	0.7134	0.6322	0.4344	0.4474	0.443
timm_jx_nest_tiny	image	0.7954	0.6187	0.5137	0.4462	0.2963
slip_vit_s_clip_yfcc15m	image	0.7157	0.5926	0.3954	0.5498	0.4115
torchvision_regnet_x_1_6gf_imagenet1k_v2	image	0.6936	0.633	0.5095	0.5539	0.275
dino_resnet50	image	0.7369	0.5882	0.5626	0.5381	0.2334
vissl_resnet50_pirl	image	0.801	0.5931	0.596	0.5421	0.1242
vissl_resnet50_swav	image	0.801	0.5931	0.596	0.5421	0.1242
vissl_resnet50_simclr	image	0.801	0.5931	0.596	0.5421	0.1242
timm_deit3_base_patch16_224	image	0.7711	0.5306	0.5734	0.4267	0.3539
slowfast_r50	video	0.6455	0.5847	0.5685	0.5601	0.2969
timm_convnext_small_in22k	image	0.8114	0.5661	0.4246	0.4373	0.4144
torchvision_swin_b_imagenet1k_v1	image	0.7516	0.5957	0.4419	0.4699	0.3912
timm_gluon_resnext101_32x4d	image	0.7298	0.6237	0.5137	0.5183	0.2619
timm_gernet_s	image	0.8253	0.6425	0.3869	0.4576	0.3211
torchvision_convnext_small_imagenet1k_v1	image	0.7602	0.5442	0.4368	0.5032	0.3876
torchvision_convnext_large_imagenet1k_v1	image	0.7316	0.6965	0.3301	0.4409	0.4271
timm_mobilenetv3_large_100_miil	image	0.7891	0.4879	0.6083	0.3781	0.3557
timm_beitv2_large_patch16_224	image	0.7984	0.6597	0.6625	0.2026	0.2928
x3d_s	video	0.7835	0.6258	0.5224	0.4451	0.2387
timm_convnext_nano	image	0.805	0.6324	0.5833	0.4811	0.1107
timm_eca_nfnet_l1	image	0.8009	0.5059	0.4996	0.2978	0.5038
timesformer-base-finetuned-k400	video	0.739	0.5617	0.5821	0.4329	0.2909
timm_convmixer_768_32	image	0.7756	0.6249	0.4804	0.3753	0.3492
timm_gluon_resnet152_v1c	image	0.7023	0.6442	0.4424	0.4935	0.3163
timm_cs3darknet_l	image	0.719	0.5842	0.4984	0.429	0.3679
torchvision_efficientnet_v2_s_imagenet1k_v1	image	0.7638	0.5872	0.4948	0.47	0.2815
timm_cs3darknet_m	image	0.7357	0.622	0.6353	0.4462	0.1573
dino_vitb8	image	0.811	0.6484	0.5523	0.3987	0.1805
torchvision_regnet_y_3_2gf_imagenet1k_v2	image	0.7257	0.6313	0.4021	0.4428	0.389
timm_cait_xs24_384	image	0.7608	0.6086	0.5349	0.464	0.2209
dino_xcit_medium_24_p16	image	0.8137	0.6187	0.5338	0.4706	0.1516
bit_expert_food	image	0.7766	0.5994	0.5448	0.5146	0.151
timm_gmlp_s16_224	image	0.7726	0.6225	0.4164	0.4129	0.362
timm_deit3_huge_patch14_224	image	0.7706	0.6328	0.4031	0.5308	0.249
timm_lamhalobotnet50ts_256	image	0.7282	0.6574	0.4391	0.463	0.2965
torchvision_regnet_y_3_2gf_imagenet1k_v1	image	0.7731	0.5932	0.3716	0.415	0.429
timm_mobilevitv2_150_384_in22ft1k	image	0.7315	0.591	0.5826	0.4657	0.2109
dino_vits16	image	0.7961	0.5373	0.6418	0.4192	0.184
torchvision_efficientnet_b1_imagenet1k_v2	image	0.7672	0.5114	0.537	0.3549	0.3995
timm_convit_base	image	0.7896	0.6389	0.4944	0.3567	0.2901
bit_expert_relation	image	0.764	0.6015	0.5572	0.5148	0.1297
vicreg_resnet50	image	0.7953	0.5523	0.5098	0.399	0.3062
timm_convit_small	image	0.7852	0.5857	0.6304	0.4463	0.1143

torchvision regnet x 400mf imagenet1k v1	image	0.6876	0.5266	0.5064	0.5594	0.2792
timm dm nfnet f0	image	0.8287	0.5191	0.5027	0.5117	0.1956
timm halonet50ts	image	0.7707	0.5389	0.4613	0.4639	0.3208
torchvision convnext_base imagenet1k v1	image	0.8279	0.6266	0.5003	0.2199	0.3762
torchvision swin t imagenet1k v1	image	0.7804	0.6604	0.3223	0.4351	0.3526
timm deit3 medium patch16 224	image	0.7488	0.5817	0.5366	0.4454	0.2373
timm ecaresnetlight	image	0.8124	0.6348	0.5852	0.3955	0.1209
torchvision regnet x 8gf imagenet1k v1	image	0.8024	0.5685	0.526	0.4123	0.2393
timm cs3sedarknet x	image	0.7975	0.5852	0.3159	0.4737	0.3744
timm cspresnext50	image	0.7068	0.5961	0.4828	0.5247	0.2316
timm cspresnet50	image	0.7698	0.5932	0.4088	0.4544	0.2995
vicreg resnet50 alpha0p9	image	0.7358	0.6036	0.5365	0.382	0.2663
timm deit3 large patch16 224 in21ft1k	image	0.8022	0.5821	0.5864	0.2696	0.2771
timm mobilenetv2 120d	image	0.7505	0.6374	0.5906	0.3917	0.1429
timm dm nfnet f3	image	0.7881	0.4862	0.4283	0.4692	0.3379
timm dla60	image	0.8025	0.6242	0.417	0.4869	0.179
torchvision efficientnet_b1 imagenet1k v1	image	0.7518	0.6215	0.4872	0.4361	0.21
timm legacy seresnet101	image	0.8245	0.6235	0.4964	0.3211	0.2388
timm deit3 medium patch16 224 in21ft1k	image	0.7849	0.6183	0.4603	0.3502	0.2904
timm dpn92	image	0.7813	0.5733	0.3913	0.4452	0.3102
timm legacy senet154	image	0.6804	0.5652	0.5131	0.4324	0.3077
timm levit 384	image	0.804	0.5437	0.5092	0.3984	0.2429
timm convnext_nano_ols	image	0.7351	0.619	0.4787	0.4321	0.2315
bit expert arthropod	image	0.7717	0.615	0.434	0.4757	0.1959
i3d_r50	video	0.6893	0.5585	0.3042	0.6122	0.3279
bit expert flower	image	0.7802	0.6004	0.4257	0.5264	0.1584
timm legacy seresnet18	image	0.7546	0.5449	0.4428	0.4646	0.2823
timm gluon_inception_v3	image	0.7515	0.6034	0.4997	0.5016	0.1312
slow_r50	video	0.7027	0.6435	0.4826	0.5279	0.1236
timm deit_tiny_distilled_patch16_224	image	0.7753	0.5786	0.4914	0.4268	0.2073
timm gluon_resnet50_v1b	image	0.7259	0.5374	0.5104	0.4234	0.2784
timm edgenet_small	image	0.797	0.5299	0.4362	0.5003	0.2084
slip_vit_s_yfcc15m	image	0.7352	0.6241	0.3496	0.5126	0.25
timm dla102x2	image	0.726	0.6423	0.3813	0.3583	0.3627
timm gluon_resnext50_32x4d	image	0.6777	0.6435	0.453	0.4427	0.2538
dino_xcit_small_12_p16	image	0.8256	0.5962	0.5035	0.391	0.1526
timm_cait_xxs24_224	image	0.7872	0.5824	0.5531	0.3378	0.2062
timm_levit_256	image	0.7598	0.6334	0.5589	0.3601	0.146
timm_convnext_xlarge_in22k	image	0.7815	0.6701	0.4171	0.4488	0.1378
bit expert bird	image	0.7765	0.6459	0.4431	0.4551	0.1335
timm_cs3edgenet_x	image	0.7224	0.6015	0.418	0.4485	0.2636
clip_rn50	image	0.7098	0.6424	0.6778	0.431	-0.0079
bit expert instrument	image	0.7695	0.6229	0.441	0.4761	0.1432
timm_beit_large_patch16_224	image	0.8185	0.6405	0.525	0.4175	0.0502
timm_botnet26t_256	image	0.6959	0.6764	0.5671	0.4458	0.0631
timm_gluon_senet154	image	0.7297	0.5644	0.4607	0.436	0.2565
dino_xcit_medium_24_p8	image	0.8166	0.654	0.5092	0.2706	0.1966
timm_convnext_xlarge_in22ft1k	image	0.7742	0.676	0.4312	0.4302	0.1333
torchvision_swin_s_imagenet1k_v1	image	0.7827	0.5631	0.4251	0.3796	0.2943
timm_dla60x	image	0.7421	0.4712	0.4524	0.4172	0.3593
timm_deit_small_patch16_224	image	0.7357	0.5909	0.4591	0.4277	0.2252
timm_gluon_seresnext50_32x4d	image	0.7044	0.6263	0.4606	0.334	0.312
timm_halo2botnet50ts_256	image	0.7638	0.5997	0.5166	0.5417	0.0141
timm_mobilevit_s	image	0.7391	0.5147	0.6189	0.384	0.1762
torchvision_regnet_x_800mf_imagenet1k_v2	image	0.7427	0.4815	0.5756	0.5719	0.0611
timm_convmixer_1024_20_ks9_p14	image	0.7908	0.6078	0.4034	0.4062	0.2243
timm_gluon_resnext101_64x4d	image	0.7593	0.6274	0.4454	0.2864	0.3139
torchvision_regnet_y_800mf_imagenet1k_v1	image	0.7351	0.537	0.3739	0.4618	0.3248
torchvision_regnet_y_1_6gf_imagenet1k_v2	image	0.8032	0.4925	0.44	0.5224	0.1731
torchvision_mobilenet_v3_large_imagenet1k_v1	image	0.8015	0.4971	0.3946	0.4185	0.3159
torchvision_mnasnet1_3_imagenet1k_v1	image	0.6932	0.5376	0.5014	0.4913	0.2035
timm_ecaresnet50d	image	0.8182	0.4872	0.3948	0.4565	0.269
timm_beit_base_patch16_384	image	0.7786	0.6621	0.5813	0.2299	0.1724

timm_dla46x_c	image	0.7421	0.5753	0.4705	0.4093	0.2252
timm_deit_base_distilled_patch16_224	image	0.8032	0.4689	0.5316	0.3953	0.2227
timm_mixer_b16_224_miil_in21k	image	0.8015	0.554	0.3198	0.4304	0.3159
torchvision_resnext101_32x8d_imagenet1k_v2	image	0.7092	0.6704	0.3667	0.5083	0.1634
timm_convit_tiny	image	0.7504	0.5993	0.5701	0.3566	0.1416
bit_expert_object	image	0.7715	0.6122	0.439	0.465	0.1277
timm_convnext_tiny_in22ft1k	image	0.7617	0.565	0.4912	0.4384	0.1574
torchvision_mobilenet_v3_small_imagenet1k_v1	image	0.7403	0.5131	0.4941	0.3639	0.3017
vissl_resnet50_deepclusterv2	image	0.7388	0.5837	0.4622	0.5423	0.086
timm_deit3_small_patch16_224	image	0.7807	0.4951	0.5107	0.5225	0.1019
timm_cs3darknet_focus_l	image	0.7019	0.5189	0.5037	0.4309	0.2546
torchvision_regnet_y_16gf_imagenet1k_v1	image	0.7523	0.4894	0.4866	0.4109	0.2683
timm_mixer_b16_224	image	0.7497	0.5962	0.3957	0.3842	0.2809
timm_mixer_b16_224_in21k	image	0.7497	0.5962	0.3957	0.3842	0.2809
timm_gluon_resnet50_v1d	image	0.8017	0.5135	0.359	0.3691	0.3626
torchvision_regnet_y_32gf_imagenet1k_v2	image	0.7402	0.5201	0.4323	0.3822	0.3308
timm_dla102x	image	0.7483	0.5859	0.475	0.4287	0.1656
timm_cs3darknet_x	image	0.7487	0.5354	0.5086	0.4163	0.1925
torchvision_swin_v2_b_imagenet1k_v1	image	0.7535	0.5072	0.4343	0.3197	0.3837
timm_levit_192	image	0.7742	0.4129	0.4963	0.546	0.1684
torchvision_regnet_y_400mf_imagenet1k_v2	image	0.7348	0.4765	0.5207	0.3067	0.3581
torchvision_shuffleNet_v2_x1_5_imagenet1k_v1	image	0.7934	0.4378	0.5218	0.4207	0.2227
timm_jx_nest_base	image	0.7851	0.5698	0.4392	0.3652	0.237
timm_mobilevitv2_150	image	0.7171	0.582	0.5419	0.3832	0.1668
bit_expert_vehicle	image	0.7666	0.6086	0.4512	0.4307	0.1335
slip_vit_s_simclr_yfcc15m	image	0.7746	0.5456	0.3739	0.4481	0.2473
timm_cspdarknet53	image	0.6817	0.5432	0.445	0.5563	0.1621
timm_densenet121	image	0.8072	0.5385	0.509	0.356	0.1766
bit_expert_abstraction	image	0.7647	0.614	0.4403	0.4436	0.121
torchvision_resnet101_imagenet1k_v1	image	0.7571	0.6102	0.3132	0.5384	0.1634
timm_gmixer_24_224	image	0.771	0.567	0.3812	0.4322	0.2306
timm_halonet26t	image	0.753	0.6144	0.5976	0.3358	0.0811
torchvision_resnet34_imagenet1k_v1	image	0.7962	0.5937	0.4995	0.2635	0.2289
torchvision_mobilenet_v2_imagenet1k_v2	image	0.7382	0.5901	0.3623	0.5305	0.1606
timm_efficientformer_l1	image	0.7476	0.5033	0.3834	0.4063	0.3403
timm_gluon_resnet50_v1c	image	0.7392	0.5382	0.528	0.4904	0.0839
timm_deit_base_distilled_patch16_384	image	0.7271	0.5959	0.4603	0.4143	0.181
timm_hardcorenas_a	image	0.7675	0.5539	0.5522	0.3712	0.1308
torchvision_regnet_y_800mf_imagenet1k_v2	image	0.7578	0.5793	0.4173	0.4179	0.2016
timm_hardcorenas_f	image	0.7561	0.5292	0.477	0.3734	0.2358
timm_cait_xxs36_384	image	0.7361	0.6453	0.5179	0.2735	0.1952
torchvision_alexnet_imagenet1k_v1	image	0.7293	0.4987	0.3443	0.429	0.3623
x3d_m	video	0.715	0.5581	0.4617	0.4364	0.1922
timm_mobilenetv3_small_075	image	0.7023	0.4729	0.4749	0.4413	0.2716
timm_deit3_small_patch16_384	image	0.7528	0.6041	0.4397	0.46	0.1036
timm_mnasnet_100	image	0.7555	0.4988	0.479	0.3969	0.2281
torchvision_regnet_x_3_2gf_imagenet1k_v2	image	0.649	0.6495	0.4706	0.5223	0.064
timm_dm_nfnet_f2	image	0.7816	0.6535	0.6721	0.3632	-0.1157
torchvision_mnasnet0_75_imagenet1k_v1	image	0.6924	0.5537	0.3551	0.4937	0.259
timm_convnext_tiny_in22k	image	0.7599	0.5338	0.3997	0.4497	0.2056
torchvision_resnext50_32x4d_imagenet1k_v2	image	0.7338	0.6331	0.5033	0.43	0.048
bit_expert_mammal	image	0.7628	0.6143	0.4818	0.3028	0.1853
timm_convnext_atto	image	0.7573	0.5465	0.5479	0.425	0.0652
vissl_resnet50_jigsaw_p100	image	0.7226	0.6083	0.374	0.4301	0.2047
timm_gluon_resnet34_v1b	image	0.7354	0.5529	0.4339	0.4282	0.1864
torchvision_regnet_y_16gf_imagenet1k_v2	image	0.8025	0.5746	0.3672	0.4175	0.174
vissl_resnet50_supervised	image	0.7944	0.5608	0.3421	0.431	0.2062
torchvision_shuffleNet_v2_x1_0_imagenet1k_v1	image	0.7659	0.4924	0.3692	0.5145	0.1909
timm_deit3_base_patch16_384	image	0.7928	0.5785	0.2467	0.4431	0.2715
timm_dla169	image	0.688	0.5638	0.4199	0.3751	0.282
timm_mobilenetv3_small_050	image	0.7077	0.4937	0.4526	0.511	0.1627
timm_efficientformer_l7	image	0.7932	0.5933	0.3583	0.388	0.1926
timm_mobilenetv3_large_100	image	0.7698	0.5315	0.422	0.5448	0.0573

bit expert animal	image	0.7687	0.6204	0.4648	0.3269	0.1436
timm deit base patch16 384	image	0.6968	0.532	0.4264	0.4596	0.2034
timm gluon resnet101 vis	image	0.7556	0.6594	0.3772	0.5938	-0.0705
timm convnext tiny hnf	image	0.7371	0.5301	0.5311	0.4448	0.0722
torchvision ssd300 vgg16 coco v1	image	0.8172	0.6585	0.4968	0.122	0.2197
timm mobilenetv2 050	image	0.7122	0.4812	0.3993	0.5127	0.2025
dino vits8	image	0.6414	0.5855	0.4134	0.4441	0.2226
timm levit 128	image	0.7982	0.4992	0.4664	0.4187	0.1214
timm deit base patch16 224	image	0.7244	0.5369	0.4038	0.4223	0.2161
slip vit b simclr yfcc15m	image	0.7786	0.5197	0.5082	0.2918	0.2026
torchvision convnext tiny imagenet1k v1	image	0.793	0.6057	0.3446	0.4262	0.1302
timm convnext tiny 384 in22ft1k	image	0.7556	0.5602	0.4162	0.3542	0.2131
torchvision shufflenet v2 x0_5 imagenet1k v1	image	0.7532	0.51	0.2573	0.5074	0.2703
torchvision mobilenet v3 large imagenet1k v2	image	0.7494	0.5056	0.4267	0.3853	0.2285
timm inception v4	image	0.7506	0.479	0.5377	0.3845	0.1431
torchvision regnet x 400mf imagenet1k v2	image	0.7256	0.5221	0.4122	0.336	0.2958
timm hardcorenas c	image	0.7854	0.4972	0.5458	0.3311	0.1299
timm edgenext small rw	image	0.7994	0.5077	0.5089	0.3336	0.1391
timm mobilenetv2 110d	image	0.7664	0.4854	0.34	0.4399	0.2471
timm haloregnetz b	image	0.7415	0.5096	0.4023	0.3559	0.2676
timm mobilevitv2 050	image	0.7624	0.555	0.4813	0.3386	0.1395
torchvision resnet18 imagenet1k v1	image	0.7803	0.543	0.4728	0.3866	0.0905
timm gluon resnet101 v1b	image	0.7229	0.6223	0.5207	0.4298	-0.0225
vissl resnet50 mocov2	image	0.7933	0.5943	0.3905	0.4162	0.0716
timm mobilenetv2 100	image	0.7642	0.5666	0.4456	0.3325	0.1563
timm gluon resnet152 v1b	image	0.7013	0.6136	0.3492	0.4133	0.1843
timm cait s24 384	image	0.7051	0.6052	0.3252	0.3104	0.3116
timm bat resnext26ts	image	0.7417	0.5857	0.16	0.4581	0.3119
timm convmixer 1536 20	image	0.7604	0.4944	0.4794	0.397	0.1191
torchvision resnext101 64x4d imagenet1k v1	image	0.6604	0.5875	0.4834	0.2365	0.2819
slip vit b clip yfcc15m	image	0.7518	0.6038	0.3355	0.4	0.1579
timm cait s36 384	image	0.7633	0.6635	0.4221	0.3462	0.0521
timm convnext small in22ft1k	image	0.7637	0.5395	0.4682	0.3447	0.13
timm ecaresnet50t	image	0.7832	0.4778	0.4326	0.4841	0.0678
timm hardcorenas e	image	0.7407	0.5263	0.4266	0.2954	0.256
timm efficientnet b0	image	0.7885	0.5128	0.539	0.2505	0.1517
torchvision resnext50 32x4d imagenet1k v1	image	0.8236	0.6071	0.1015	0.4661	0.2406
timm mobilevit xxs	image	0.8066	0.5449	0.4466	0.3296	0.1093
timm mobilevit xs	image	0.7874	0.5761	0.4698	0.2662	0.1372
timm eca resnet33ts	image	0.7545	0.5112	0.493	0.2616	0.2144
timm mobilenetv3 large 100 miil in21k	image	0.771	0.5731	0.4246	0.4785	-0.0131
torchvision resnet152 imagenet1k v1	image	0.801	0.4099	0.4077	0.1697	0.4442
torchvision shufflenet v2 x2_0 imagenet1k v1	image	0.7131	0.5295	0.5435	0.5033	-0.0571
timm gluon resnet152 v1d	image	0.7135	0.6344	0.2567	0.5372	0.0901
timm efficientnet b2	image	0.7822	0.5356	0.4069	0.2725	0.2284
timm inception resnet v2	image	0.7791	0.6238	0.4585	0.2774	0.0865
timm ghostnet 100	image	0.7976	0.5858	0.5587	0.3405	-0.0625
torchvision ssdlite320 mobilenet v3 large coco v1	image	0.768	0.6451	0.272	0.4239	0.1107
timm mobilevitv2 150 in22ft1k	image	0.731	0.477	0.3362	0.348	0.3272
timm hardcorenas d	image	0.7333	0.5149	0.4268	0.3583	0.1859
timm convnext pico ols	image	0.7656	0.5545	0.4077	0.3986	0.0919
timm ig resnext101 32x32d	image	0.7226	0.5594	0.295	0.4756	0.1656
timm ig resnext101 32x16d	image	0.7226	0.5594	0.295	0.4756	0.1656
timm ig resnext101 32x8d	image	0.7226	0.5594	0.295	0.4756	0.1656
timm ig resnext101 32x48d	image	0.7226	0.5594	0.295	0.4756	0.1656
timm cait xxs24 384	image	0.7873	0.5839	0.5085	0.4054	-0.0681
timm levit 128s	image	0.7554	0.5405	0.4035	0.4176	0.0976
timm eca resnext26ts	image	0.6497	0.5038	0.5106	0.4016	0.148
timm mobilevitv2 075	image	0.7319	0.5445	0.5424	0.2557	0.1384
timm densenet201	image	0.7133	0.5673	0.318	0.358	0.256
torchvision resnet101 imagenet1k v2	image	0.7214	0.56	0.4893	0.5135	-0.074
timm mobilevitv2 125	image	0.7384	0.5104	0.4966	0.3304	0.1315
timm dm nfnet f4	image	0.7683	0.4679	0.3572	0.4799	0.1328

timm_mixer_l16_224_in21k	image	0.7466	0.5074	0.3161	0.3135	0.3198
timm_mixer_l16_224	image	0.7466	0.5074	0.3161	0.3135	0.3198
torchvision_regnet_y_400mf_imagenet1k_v1	image	0.7413	0.4935	0.5198	0.3791	0.0667
timm_dla102	image	0.7092	0.6133	0.3882	0.3459	0.1408
torchvision_regnet_y_8gf_imagenet1k_v2	image	0.7012	0.4944	0.4507	0.4229	0.1281
timm_convnext_femto_ols	image	0.778	0.4716	0.3481	0.4967	0.0992
timm_convnext_atto_ols	image	0.7274	0.4354	0.5295	0.3632	0.1339
timm_dla46_c	image	0.8216	0.5016	0.4258	0.422	0.0136
timm_hardcorenas_b	image	0.7388	0.4791	0.5284	0.308	0.1228
timm_gluon_resnet101_v1d	image	0.6434	0.5673	0.2849	0.4331	0.2416
torchvision_regnet_x_16gf_imagenet1k_v2	image	0.7278	0.5014	0.4388	0.3486	0.1519
timm_gluon_resnet18_v1b	image	0.752	0.5442	0.3602	0.3535	0.1578
torchvision_regnet_x_3_2gf_imagenet1k_v1	image	0.7178	0.4522	0.3204	0.4663	0.2081
timm_lcnet_100	image	0.7827	0.536	0.4504	0.2069	0.1881
timm_mvitv2_base	image	0.7543	0.5704	0.5032	0.4639	-0.129
timm_inception_v3	image	0.7661	0.4786	0.2779	0.4788	0.1603
timm_mobilenetv3_rw	image	0.7691	0.5035	0.3319	0.4195	0.1361
torchvision_resnext101_32x8d_imagenet1k_v1	image	0.7762	0.5754	0.1969	0.3776	0.231
timm_ecaresnet26t	image	0.7326	0.5678	0.3292	0.4777	0.0486
timm_cs3darknet_focus_m	image	0.7961	0.5371	0.4674	0.4917	-0.1446
timm_legacy_seresnet34	image	0.7835	0.6036	0.3491	0.4289	-0.019
timm_densenet169	image	0.5511	0.5115	0.4031	0.4615	0.2091
timm_efficientnet_b1	image	0.6615	0.4573	0.4815	0.4198	0.1113
torchvision_mobilenet_v2_imagenet1k_v1	image	0.7786	0.4402	0.3555	0.426	0.1211
timm_lambda_resnet26rpt_256	image	0.7237	0.6085	0.2321	0.4881	0.0657
dino_vitb16	image	0.8148	0.548	0.0886	0.4409	0.2221
timm_ecaresnet269d	image	0.742	0.5016	0.5273	0.2732	0.069
torchvision_densenet169_imagenet1k_v1	image	0.5514	0.5263	0.3956	0.4376	0.2022
timm_dla34	image	0.7551	0.5184	0.4438	0.312	0.0829
timm_lcnet_075	image	0.7438	0.5293	0.3299	0.2675	0.2405
vissl_resnet50_clusterfit	image	0.7686	0.5662	0.2448	0.3935	0.1299
torchvision_densenet121_imagenet1k_v1	image	0.6889	0.5022	0.4292	0.358	0.1204
timm_mobilenetv2_140	image	0.7526	0.4949	0.2789	0.4348	0.1327
torchvision_regnet_y_8gf_imagenet1k_v1	image	0.7942	0.5928	0.3096	0.4036	-0.0094
timm_edgenet_xx_small	image	0.7944	0.5335	0.5147	0.1278	0.1205
timm_deit_tiny_patch16_224	image	0.7285	0.4965	0.4339	0.2595	0.1673
timm_darknet53	image	0.6459	0.6054	0.2323	0.4527	0.1483
timm_ecaresnet101d	image	0.836	0.533	0.3541	0.223	0.1377
timm_legacy_seresnext26_32x4d	image	0.7734	0.562	0.3535	0.3331	0.0612
timm_gluon_seresnext101_64x4d	image	0.8212	0.604	0.3698	0.5227	-0.2389
timm_gluon_seresnext101_32x4d	image	0.7768	0.4124	0.143	0.4789	0.263
timm_lcnet_050	image	0.6679	0.4597	0.3826	0.2207	0.3386
timm_dla60x_c	image	0.7786	0.5474	0.2899	0.2251	0.2277
timm_darknetaa53	image	0.7266	0.5523	0.2712	0.5034	0.0058
torchvision_mnasnet0_5_imagenet1k_v1	image	0.7479	0.4795	0.4128	0.4231	-0.0075
timm_mnasnet_small	image	0.6649	0.5395	0.607	0.0358	0.2076
vissl_resnet50_jigsaw_goyal19	image	0.7013	0.5397	0.3567	0.4384	0.0126
timm_mixnet_m	image	0.7943	0.4956	0.3089	0.2048	0.2423
vissl_resnet50_rotnet	image	0.701	0.5713	0.1629	0.3847	0.2184
timm_cs3sedarknet_l	image	0.7197	0.4533	0.4444	0.3519	0.0681
timm_convnext_femto	image	0.7797	0.4834	0.1975	0.3765	0.181
torchvision_resnet50_imagenet1k_v1	image	0.7322	0.477	0.28	0.3623	0.1555
dino_xcit_small_l2_p8	image	0.8229	0.6776	0.4106	0.3279	-0.2367
timm_jx_nest_small	image	0.7662	0.6071	0.565	0.209	-0.1565
torchvision_regnet_y_32gf_imagenet1k_v1	image	0.7467	0.454	0.2998	0.1169	0.3332
torchvision_densenet201_imagenet1k_v1	image	0.7144	0.5664	0.3134	0.3475	0.006
torchvision_inception_v3_imagenet1k_v1	image	0.7665	0.4812	0.2544	0.2836	0.161
timm_eca_nfnet_l2	image	0.7934	0.3318	0.186	0.2123	0.4089
timm_lambda_resnet50ts	image	0.7441	0.6037	0.1522	0.3766	0.042
timm_gluon_resnet152_v1s	image	0.6594	0.4908	0.3589	0.3501	0.041
timm_mobilenetv3_small_100	image	0.732	0.574	0.4958	-0.0076	0.0777
timm_mobilevitv2_100	image	0.7801	0.5201	0.1054	0.3113	0.1447
timm_mixnet_s	image	0.7424	0.5093	0.3785	0.2781	-0.0468

timm_legacy_seresnext101_32x4d	image	0.6634	0.4777	0.3745	0.1255	0.2168
torchvision_squeezenet1_0_imagenet1k_v1	image	0.6452	0.4969	0.3821	0.171	0.1235
timm_legacy_seresnet152	image	0.812	0.6272	0.0837	0.0999	0.1531
timm_densenet161	image	0.666	0.4925	0.2929	0.3532	-0.0611
torchvision_squeezenet1_1_imagenet1k_v1	image	0.7709	0.429	0.2259	0.2374	0.0797
torchvision_resnet152_imagenet1k_v2	image	0.6981	0.572	0.2959	0.2435	-0.0836
timm_cs3se_edgenet_x	image	0.772	0.6367	0.0091	0.2194	0.0789
torchvision_regnet_x_8gf_imagenet1k_v2	image	0.6967	0.5006	0.3604	-0.0054	0.161
c2d_r50	video	0.6384	0.5905	0.1191	0.1476	0.1294
torchvision_regnet_y_1_6gf_imagenet1k_v1	image	0.7651	0.4819	0.429	0.2633	-0.3227
timm_efficientformer_l3	image	0.8125	0.5459	0.0514	-0.132	0.1477
torchvision_densenet161_imagenet1k_v1	image	0.6656	0.493	0.3019	-0.0464	-0.0809

Supplemental Table 1: List of Vision DNNs Tested. This table provides a complete list of all pretrained image and video deep neural networks included in our analysis, ranked by their performance on the average score across five ratings.

Reference

Abassi, E., & Papeo, L. (2020). The Representation of Two-Body Shapes in the Human Visual

Cortex. Journal of Neuroscience, 40(4), 852–863.

<https://doi.org/10.1523/JNEUROSCI.1378-19.2019>

Bao, H., Dong, L., Piao, S., & Wei, F. (2021). Beit: Bert pre-training of image transformers.

arXiv Preprint arXiv:2106.08254.

Bertasius, G., Wang, H., & Torresani, L. (2021). *Is Space-Time Attention All You Need for Video*

Understanding? (No. arXiv:2102.05095). arXiv.

<https://doi.org/10.48550/arXiv.2102.05095>

Bowers, J. S., Malhotra, G., Dujmović, M., Montero, M. L., Tsvetkov, C., Biscione, V., Puebla,

G., Adolphi, F., Hummel, J. E., Heaton, R. F., Evans, B. D., Mitchell, J., & Blything, R.

(2023). Deep problems with neural network models of human vision. *Behavioral and*

Brain Sciences, 46, e385. <https://doi.org/10.1017/S0140525X22002813>

Chen, T., Kornblith, S., Norouzi, M., & Hinton, G. (2020). *A Simple Framework for Contrastive*

Learning of Visual Representations (No. arXiv:2002.05709). arXiv.

<https://doi.org/10.48550/arXiv.2002.05709>

- Conwell, C., Prince, J. S., Kay, K. N., Alvarez, G. A., & Konkle, T. (2024). A large-scale examination of inductive biases shaping high-level visual representation in brains and machines. *Nature Communications*, *15*(1), 9383. <https://doi.org/10.1038/s41467-024-53147-y>
- Downing, P. E., Jiang, Y., Shuman, M., & Kanwisher, N. (2001). A Cortical Area Selective for Visual Processing of the Human Body. *Science*, *293*(5539), 2470–2473. <https://doi.org/10.1126/science.1063414>
- Dupré la Tour, T., Eickenberg, M., Nunez-Elizalde, A. O., & Gallant, J. L. (2022). Feature-space selection with banded ridge regression. *NeuroImage*, *264*, 119728. <https://doi.org/10.1016/j.neuroimage.2022.119728>
- Feichtenhofer, C. (2020). *X3D: Expanding Architectures for Efficient Video Recognition* (No. arXiv:2004.04730). arXiv. <https://doi.org/10.48550/arXiv.2004.04730>
- Feichtenhofer, C., Fan, H., Malik, J., & He, K. (2019). *SlowFast Networks for Video Recognition* (No. arXiv:1812.03982). arXiv. <https://doi.org/10.48550/arXiv.1812.03982>
- Gandolfo, M., Abassi, E., Balgova, E., Downing, P. E., Papeo, L., & Koldewyn, K. (2024). Converging evidence that left extrastriate body area supports visual sensitivity to social interactions. *Current Biology*, *34*(2), 343-351.e5. <https://doi.org/10.1016/j.cub.2023.12.009>
- Garcia, K., McMahon, E., Conwell, C., Bonner, M. F., & Isik, L. (2024). *Modeling dynamic social vision highlights gaps between deep learning and humans*. PsyArXiv. <https://doi.org/10.31234/osf.io/4mpd9>
- Goel, S., Pavlakos, G., Rajasegaran, J., Kanazawa, A., & Malik, J. (2023). *Humans in 4D: Reconstructing and Tracking Humans with Transformers*. 14783–14794.

https://openaccess.thecvf.com/content/ICCV2023/html/Goel_Humans_in_4D_Reconstructing_and_Tracking_Humans_with_Transformers_ICCV_2023_paper.html

Goyal, P., Duval, Q., Reizenstein, J., Leavitt, M., Xu, M., Lefaudeux, B., Singh, M., Reis, V., Caron, M., Bojanowski, P., Joulin, A., & Misra, I. (2021). *VISSL*.

<https://github.com/facebookresearch/vissl>

Hafri, A., & Firestone, C. (2021). The Perception of Relations. *Trends in Cognitive Sciences*, 25(6), 475–492. <https://doi.org/10.1016/j.tics.2021.01.006>

Hafri, A., Papafragou, A., & Trueswell, J. C. (2013). Getting the gist of events: Recognition of two-participant actions from brief displays. *Journal of Experimental Psychology: General*, 142(3), 880–905. <https://doi.org/10.1037/a0030045>

Hamlin, J. K., Wynn, K., & Bloom, P. (2007). Social evaluation by preverbal infants. *Nature*, 450(7169), 557–559. <https://doi.org/10.1038/nature06288>

Krupenye, C., & Hare, B. (2018). Bonobos Prefer Individuals that Hinder Others over Those that Help. *Current Biology: CB*, 28(2), 280–286.e5. <https://doi.org/10.1016/j.cub.2017.11.061>

Lake, B. M., Ullman, T. D., Tenenbaum, J. B., & Gershman, S. J. (2017). Building machines that learn and think like people. *Behavioral and Brain Sciences*, 40, e253. <https://doi.org/10.1017/S0140525X16001837>

Larsen, K. G., & Nelson, J. (2014). *The Johnson-Lindenstrauss lemma is optimal for linear dimensionality reduction* (No. arXiv:1411.2404). arXiv.

<https://doi.org/10.48550/arXiv.1411.2404>

Malik, M., & Isik, L. (2023). Relational visual representations underlie human social interaction recognition. *Nature Communications*, 14(1), 7317. <https://doi.org/10.1038/s41467-023-43156-8>

- McCloskey, M. (1991). Networks and Theories: The Place of Connectionism in Cognitive Science. *Psychological Science*, 2(6), 387–395. <https://doi.org/10.1111/j.1467-9280.1991.tb00173.x>
- McMahon, E., Bonner, M. F., & Isik, L. (2023). Hierarchical organization of social action features along the lateral visual pathway. *Current Biology: CB*, 33(23), 5035-5047.e8. <https://doi.org/10.1016/j.cub.2023.10.015>
- McMahon, E., & Isik, L. (2023). Seeing social interactions. *Trends in Cognitive Sciences*, 27(12), 1165–1179. <https://doi.org/10.1016/j.tics.2023.09.001>
- Monfort, M., Andonian, A., Zhou, B., Ramakrishnan, K., Bargal, S. A., Yan, T., Brown, L., Fan, Q., Gutfreund, D., Vondrick, C., & Oliva, A. (2020). Moments in Time Dataset: One Million Videos for Event Understanding. *IEEE Transactions on Pattern Analysis and Machine Intelligence*, 42(2), 502–508. <https://doi.org/10.1109/TPAMI.2019.2901464>
- Netanyahu, A., Shu, T., Katz, B., Barbu, A., & Tenenbaum, J. B. (2021). *PHASE: PHysically-grounded Abstract Social Events for Machine Social Perception* (No. arXiv:2103.01933). arXiv. <https://doi.org/10.48550/arXiv.2103.01933>
- Papeo, L. (2020). Twos in human visual perception. *Cortex; a Journal Devoted to the Study of the Nervous System and Behavior*, 132, 473–478. <https://doi.org/10.1016/j.cortex.2020.06.005>
- Pavlakos, G., Choutas, V., Ghorbani, N., Bolkart, T., Osman, A. A. A., Tzionas, D., & Black, M. J. (2019). Expressive Body Capture: 3D Hands, Face, and Body from a Single Image. *Proceedings IEEE Conf. on Computer Vision and Pattern Recognition (CVPR)*.

- Qin, W., Malik, M., & Isik, L. (2025). Relational Information Predicts Human Behavior and Neural Responses to Complex Social Scenes. *Proceedings of the Annual Meeting of the Cognitive Science Society*, 47(0). <https://escholarship.org/uc/item/4680v4ws>
- Radford, A., Kim, J. W., Hallacy, C., Ramesh, A., Goh, G., Agarwal, S., Sastry, G., Askell, A., Mishkin, P., Clark, J., Krueger, G., & Sutskever, I. (2021). *Learning Transferable Visual Models From Natural Language Supervision* (No. arXiv:2103.00020). arXiv. <https://doi.org/10.48550/arXiv.2103.00020>
- Scholl, B. J., & Gao, T. (2013). Perceiving animacy and intentionality: Visual processing or higher-level judgment? In *Social perception: Detection and interpretation of animacy, agency, and intention* (pp. 197–229). Boston Review. <https://doi.org/10.7551/mitpress/9780262019279.003.0009>
- Shu, T., Bhandwaldar, A., Gan, C., Smith, K. A., Liu, S., Gutfreund, D., Spelke, E., Tenenbaum, J. B., & Ullman, T. D. (2021). *AGENT: A Benchmark for Core Psychological Reasoning* (No. arXiv:2102.12321). arXiv. <https://doi.org/10.48550/arXiv.2102.12321>
- Spelke, E. S. (2022). Core Social Cognition. In E. S. Spelke (Ed.), *What Babies Know: Core Knowledge and Composition Volume 1* (p. 0). Oxford University Press. <https://doi.org/10.1093/oso/9780190618247.003.0008>
- Sun, Y., Liu, W., Bao, Q., Fu, Y., Mei, T., & Black, M. J. (2022). Putting People in their Place: Monocular Regression of 3D People in Depth. *2022 IEEE/CVF Conference on Computer Vision and Pattern Recognition (CVPR)*, 13233–13242. <https://doi.org/10.1109/CVPR52688.2022.01289>

Thomas, A. J. (2024). Cognitive Representations of Social Relationships and their Developmental Origins. *Behavioral and Brain Sciences*, 1–53.

<https://doi.org/10.1017/S0140525X24001328>

TorchVision maintainers and contributors. (2016). TorchVision: PyTorch's Computer Vision library. In *GitHub repository* [Computer software]. GitHub.

<https://github.com/pytorch/vision>

Wightman, R. (2019). PyTorch Image Models. In *GitHub repository*. GitHub.

<https://doi.org/10.5281/zenodo.4414861>

Zhou, C., Han, M., Liang, Q., Hu, Y.-F., & Kuai, S.-G. (2019). A social interaction field model accurately identifies static and dynamic social groupings. *Nature Human Behaviour*, 3(8),

847–855. <https://doi.org/10.1038/s41562-019-0618-2>

Zhu, H., Ge, Y., Bratch, A., Yuille, A., Kay, K., & Kersten, D. (2024). Natural scenes reveal diverse representations of 2D and 3D body pose in the human brain. *Proceedings of the National Academy of Sciences*, 121(24), e2317707121.

<https://doi.org/10.1073/pnas.2317707121>